Materials Today Bio 31 (2025) 101554

Contents lists available at ScienceDirect

Materials Today Bio

journal homepage: www.journals.elsevier.com/materials-today-bio

Photothermal-controlled microneedle for transdermal delivery of metal-phenolic nanozyme with staged multifunctions to accelerate healing of infected diabetic wounds

Dong Yan [a,b], Guoqi Cao [a,b], Yikai Gao [e], Yiping Wang [f], Wenqiang Zhang [a,b], Kun Wang [a,b], Shumei Mao [g], Chengde Li [g], Guangdong Zhou [c], Huitang Xia [a,b,c,**], Wufei Dai [c,h,*], Xiaoyu Yan [d,***], Yibing Wang [a,b,****]

[a] Department of Plastic Surgery, Shandong Provincial Qianfoshan Hospital, Shandong University, Jinan, 250012, PR China
[b] Jinan Clinical Research Center for Tissue Engineering Skin Regeneration and Wound Repair, Jinan, 250014, PR China
[c] Shanghai Key Lab of Tissue Engineering, Shanghai 9th People's Hospital, Shanghai Jiao Tong University School of Medicine, Shanghai, 200011, PR China
[d] Department of Sports Medicine, Department of Orthopedics, Shanghai Jiao Tong University Affiliated Sixth People's Hospital, Shanghai, 200233, PR China
[e] Department of Ultrasound Intervention, Shandong Provincial Third Hospital, Shandong University, Jinan, 250031, PR China
[f] Department of Radiology, Qilu Hospital of Shandong University, Shandong University, 107 Wenhua West Road, Lixia District, Jinan City, Shandong Province, 250014, PR China
[g] Department of Clinical Pharmacy, Weifang Medical University, Weifang, 261053, PR China
[h] Department of Medicine 1, Universitätsklinikum Erlangen, Friedrich-Alexander-Universität Erlangen-Nürnberg (FAU), Erlangen, 91054, Germany

ARTICLE INFO

Keywords:
Photothermal-controllable
Metal-phenolic nanozyme
Transdermal delivery
Staged multifunction
Wound healing

ABSTRACT

Conventional wound dressings for infected diabetic wounds (IDWs) typically target only the wound surface, often neglecting the need for multifunctional therapies that address deeper tissue layers, resulting in less effective treatment outcomes. Emerging research suggests that a comprehensive approach to IDW therapy should involve the transdermal delivery of therapeutic agents capable of staged bacterial eradication, reactive oxygen species (ROS) scavenging, and angiogenesis. This study introduces a novel metal-phenolic nanozyme, CuTA@MnO_2 nanoflake, designed for transdermal delivery in IDW therapy. The nanozyme is synthesized by loading copper ions (Cu^{2+}) onto manganese dioxide (MnO_2) via in-situ polymerization, with tannic acid (TA) as a linker, and encapsulated in a hyaluronic acid (HA) solution to form a photothermally controlled microneedle system. In a IDW rat model, this system effectively delivered photothermal therapy, eliminating bacteria under 808 nm near-infrared light. The heat-induced HA degradation released the CuTA@MnO_2 nanoflake, where MnO_2 and TA reduced ROS levels, providing antioxidant effects. Concurrently, released Cu^{2+} promoted angiogenesis, significantly accelerating wound healing. Whole transcriptome RNA sequencing confirmed that the CuTA@MnO_2 microneedle enhanced angiogenesis and collagen remodeling, along with reduced inflammation. The CuTA@MnO_2 microneedle offers a promising platform for the staged treatment of IDWs through bacterial eradication, oxidant scavenging, and angiogenesis promotion.

1. Introduction

Approximately 25 % of diabetic patients suffer from non-healing wounds [1]. These wounds are more susceptible to bacterial infections due to impaired immune responses caused by chronic hyperglycemia [2]. High blood sugar levels weaken the body's ability to fight infections by reducing blood circulation and causing nerve damage. These factors create a favorable environment for bacterial growth. Additionally,

* Corresponding author. Shanghai Key Lab of Tissue Engineering, Shanghai 9th People's Hospital, Shanghai Jiao Tong University School of Medicine, Shanghai, 200011, PR China.
** Corresponding author. Department of Plastic Surgery, Shandong Provincial Qianfoshan Hospital, Shandong University, Jinan, 250012, PR China.
*** Corresponding author.
**** Corresponding author. Department of Plastic Surgery, Shandong Provincial Qianfoshan Hospital, Shandong University, Jinan, 250012, PR China.
E-mail addresses: xiahuitang@163.com (H. Xia), Wufei.Dai@extern.uk-erlangen.de (W. Dai), xyyan@sjtu.edu.cn (X. Yan), ybwang@sdfmu.edu.cn (Y. Wang).

https://doi.org/10.1016/j.mtbio.2025.101554
Received 12 December 2024; Received in revised form 26 January 2025; Accepted 3 February 2025
Available online 4 February 2025

diabetic wounds are prone to excessive accumulation of reactive oxygen species (ROS) due to impaired glucose metabolism, leading to oxidative stress and cellular damage [3]. Diabetic conditions often involve weakened antioxidant defenses, which exacerbate ROS buildup [4]. Moreover, hyperglycemia thickens and stiffens blood vessels, reducing blood flow to the wound site, and further complicating healing [5]. Current clinical treatments for infected diabetic wounds (IDWs) include debridement, topical antibiotics, negative pressure wound therapy, hyperbaric oxygen therapy, and the use of growth factors and stem cells [6]. However, these methods are often inadequate due to persistent bacterial colonization, ROS accumulation, and poor blood circulation, making IDWs particularly challenging to treat.

Recent advances in biomaterial-based regenerative medicine have proposed multifunctional wound dressings, such as hydrocolloids, hydrogels, and foam dressings, which maintain a moist wound environment to promote healing [7]. However, most of these dressings are applied only to the wound surface, posing significant limitations in treating IDWs: 1) Surface-applied drugs struggle to penetrate the skin's natural barrier, making it difficult for the medication to reach deeper tissues, thereby failing to effectively promote wound repair and regeneration. 2) Surface-applied drugs may quickly evaporate or be removed, resulting in a short duration of efficacy. Frequent reapplication can lead to drug wastage and skin irritation. 3) Surface treatments do not address underlying issues such as poor blood supply and excessive ROS accumulation, which may slow the healing process and increase the risk of infection and complications [8]. As a result, relying solely on surface drug treatments often falls short of achieving optimal results for IDW healing [9].

Increasing evidence suggests that transdermal delivery of therapeutic agents into deep wound tissues can significantly improve treatment effectiveness [10]. Recent studies indicate that microneedles with carefully designed lengths can penetrate the epidermal barrier and deliver therapeutic agents directly into the deeper skin layers, reaching the dermis or even the subdermal tissue where they can effectively target damaged tissues [11]. The length of the microneedles is crucial: microneedles shorter than 100 μm may only reach the stratum corneum, while microneedles with a length of 300–1000 μm are necessary to penetrate below the epidermal layer into the dermis, where they can effectively enhance drug retention and facilitate better therapeutic outcomes. This direct access to the deeper layers of the skin ensures that the therapeutic agents reach the site of injury, promoting faster and more efficient healing. By targeting the dermis, microneedles not only enhance the retention of the therapeutic agents at the wound site but also ensure a sustained release over time. Moreover, microneedles cause minimal discomfort and avoid the large punctures or incisions associated with traditional needle-based methods, reducing infection risk and promoting faster recovery [12]. The micro-sized tips create tiny channels in the skin, significantly enhancing drug absorption and efficacy, especially in areas with poor blood circulation typical of IDWs [13]. Furthermore, microneedles can be tailored to deliver various therapeutic agents, including growth factors, antibiotics, and anti-inflammatory drugs, making them versatile for different aspects of IDW treatment [14]. These advantages make microneedles a promising and necessary tool for enhancing IDW healing.

IDW healing is a complex, multi-stage process, with each stage requiring different biological effects to work in concert [15]. Given that IDW healing is often compromised by bacterial infection, impaired blood supply, and poor collagen deposition, precise regulation of these effects is crucial to overcoming these challenges and promoting more effective healing [16]. Thus, a strategy that enables transdermal delivery of multifunctional therapeutic agents into the wound, providing staged antibacterial, antioxidant, and angiogenic effects, is highly desirable. To meet these needs, it is urgently necessary to identify suitable multifunctional therapeutic agents with these staged effects that can be loaded into a microneedle.

As a novel metal-phenolic nanoenzyme, manganese dioxide (MnO_2) has demonstrated antibacterial activity in response to near-infrared (NIR) illumination, making it beneficial for eliminating infections in IDWs [17]. Additionally, MnO_2 nanoflakes possess intrinsic antioxidant properties that can neutralize ROS [18]. This capability mitigates oxidant stress and supplies oxygen necessary for wound rehabilitation, positioning MnO_2 as a potential therapeutic agent to treat IDW. Moreover, copper ions (Cu^{2+}) can upregulate the expression of key angiogenic factors, such as vascular endothelial growth factor (VEGF) and fibroblast growth factor [19]. These factors stimulate endothelial cell proliferation and migration, essential for new blood vessel formation. Tannic acid (TA), a natural polyphenol with multiple phenolic hydroxyl groups, can form stable complexes with metal ions [20]. This property makes it feasible to use TA as an intermediary for loading Cu onto MnO_2 nanoflakes, resulting in multifunctional nanoflakes with antibacterial action upon NIR illumination, along with ROS scavenging and angiogenic activities.

Consequently, this study proposes the development of a new metal-phenolic nanozyme, CuTA@MnO_2 nanoflake, created through an in-situ polymerization process. In this process, Cu^{2+} are grafted onto the surface of MnO_2 nanoflakes with the assistance of TA. The resulting nanozyme exhibits staged antibacterial, antioxidant, and pro-angiogenesis functions. To ensure deep delivery of therapeutic agents into wound tissues, we designed a methacrylated hyaluronic acid (HA) microneedle to encapsulate the CuTA@MnO_2 nanoflake, forming a photothermal-controlled multifunctional CuTA@MnO_2 microneedle, as illustrated in Scheme 1. Upon NIR illumination, the CuTA@MnO_2

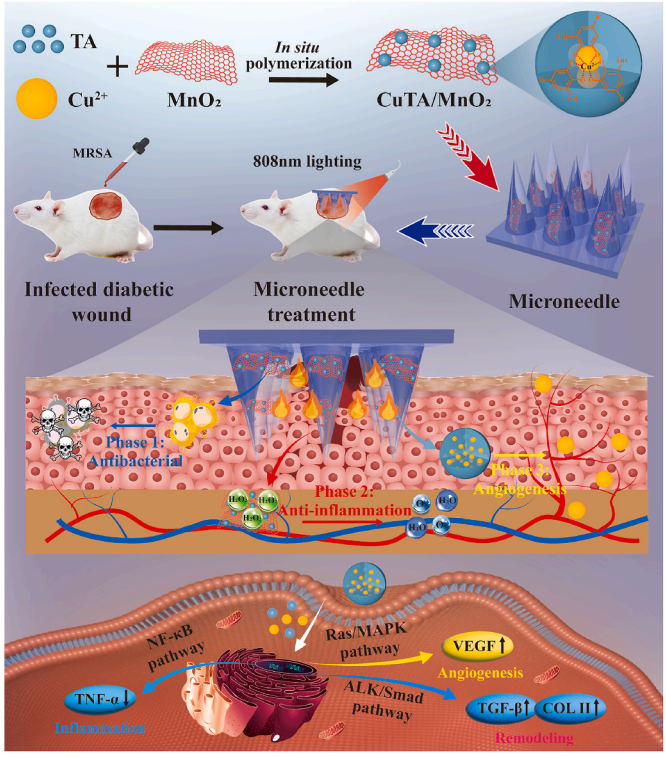

Scheme 1. Overall schematic diagram. TA and Cu were grafted onto MnO_2 nanoflakes using in-situ polymerization to obtain CuTA@MnO_2 nanoflakes via a one-step process. Thereafter, the CuTA@MnO_2 nanoflakes were encapsulated into a HA-derived microneedle. The CuTA@MnO_2 microneedle was deeply inserted into the IDW in a rat model for transdermal therapy. Upon NIR illumination using 808 nm light, the CuTA@MnO_2 microneedle is overheated to combat bacteria. In addition, the hyperthermia effectively accelerates the release of MnO_2, TA, and Cu from the CuTA@MnO_2 microneedle, in which the MnO_2 nanoflakes and TA could then synergistically scavenge ROS to exert an antioxidant effect, and the later released Cu facilitates angiogenesis, thus expediting IDW healing.

microneedle rapidly eliminates bacteria via the photothermal effect. The induced hyperthermia subsequently promotes the decomposition of CuTA@MnO_2 nanoflakes, releasing MnO_2 and Cu^{2+} to scavenge excess ROS and facilitate vascularization. These chronologically orchestrated effects are expected to significantly accelerate IDW healing.

2. Results and discussion

2.1. Characterizations of CuTA@MnO_2 nanoflakes

CuTA nanoparticles were initially synthesized through oxidative coupling assembly using $CuSO_4{\cdot}5H_2O$ and TA. Scanning electron microscopy (SEM) images confirmed the nanostructured morphology of the CuTA nanoenzyme (Fig. 1A). Next, CuTA@MnO_2 nanoflakes were synthesized via in-situ polymerization, where MnO_2 nanoflakes was surficial modified with Cu^{2+} using intermediary TA. Transmission electron microscopy (TEM) images verified the characteristic two-dimensional (2D) nanoflake structure of MnO_2 (Fig. 1B). Despite the significant loading of CuTA nanoparticles, the MnO_2 nanoflake structure remained intact (Fig. 1C), indicating that the surface modification with CuTA did not alter the MnO_2 nanoflake structure. Closer TEM view confirmed the existence of CuTA on the CuTA@MnO_2 nanoflakes (Fig. 1D). Elemental mapping demonstrated successful surface modification, in view of the detection of Mn, O, C, H, and Cu elements within the CuTA@MnO_2 nanoflakes (Fig. 1E).

The X-ray diffraction (XRD) pattern displayed sharp diffraction peaks of CuTA nanoparticles, indicative of a well-defined crystalline structure (Fig. 1F). The diffraction the peaks at 12.55°, 25.24°, and 37.31° are respectively corresponded to the (001), (002), and (−111) planes of crystal structure of MnO_2 nanosheets. The chemical composition of the CuTA nanoparticles was further analyzed using X-ray photoelectron spectroscopy (XPS). The wide scan spectra confirmed the presence of Cu, O, and C, without any additional signals (Fig. 1G). Fourier-transform infrared spectroscopy (FTIR) spectroscopy revealed that, compared to TA, the absorption peak centered at 3380 cm^{-1} was split, and peaks in the fingerprint region were shifted in the CuTA nanoparticle spectra (Fig. 1H). This shift suggests that coordination between the phenolic groups in TA and Cu^{2+} ions disrupted the C−OH vibration of TA. Additionally, the FTIR spectrum of CuTA@MnO_2 displayed both the characteristic peaks of MnO_2 and CuTA (Fig. 1I), with the absorption

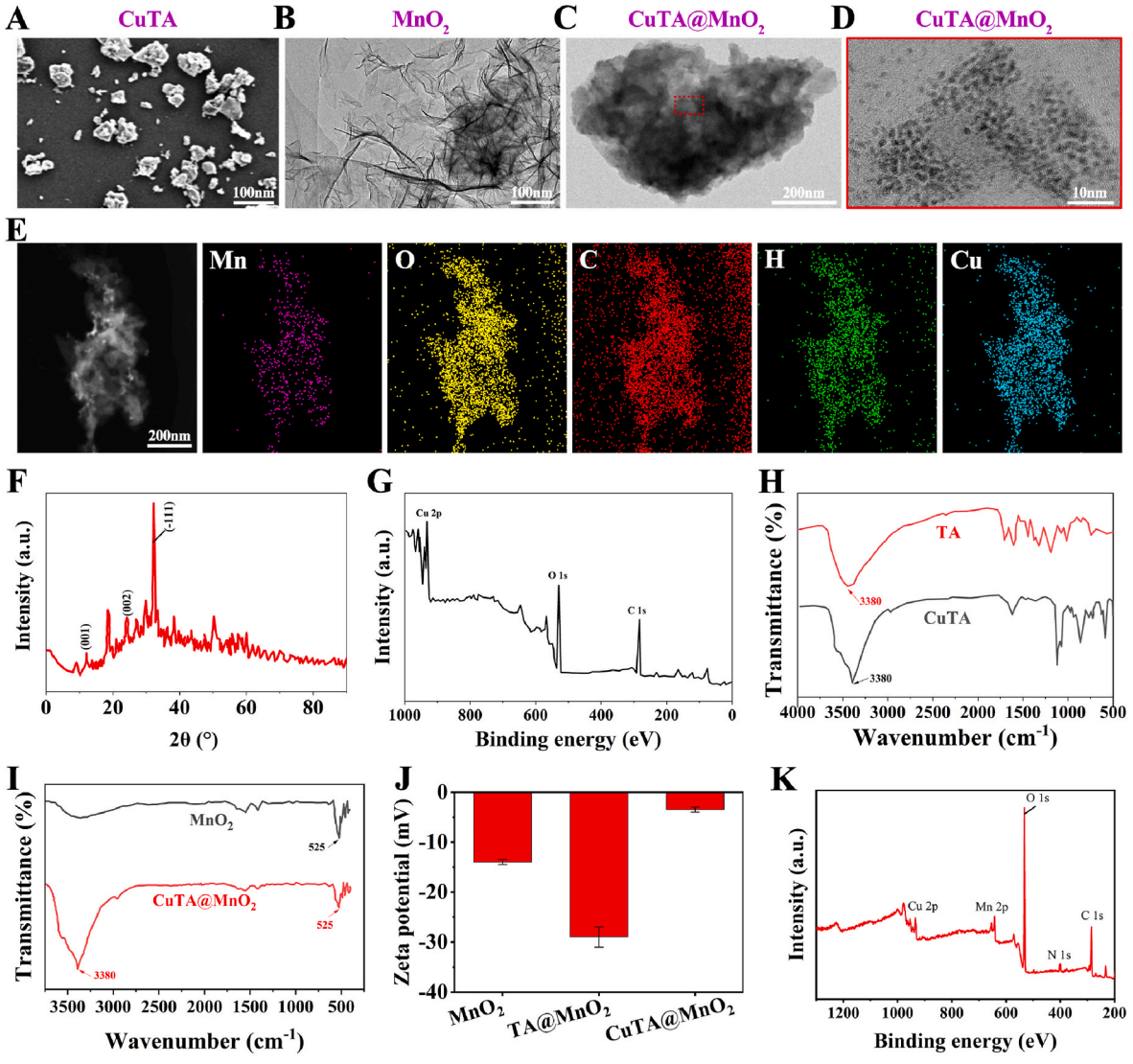

Fig. 1. The development of CuTA@MnO_2 nanoflake. A) SEM image of CuTA nanoparticles. B) TEM image of MnO_2 nanoflake. C) TEM and D) its magnification images of CuTA@MnO_2 nanoflake. E) Elemental mapping for CuTA@MnO_2 nanoflake. F) XRD pattern and G) XPS spectra of CuTA nanoparticle. H) FTIR spectra of TA and CuTA samples. I) FTIR spectra for MnO_2 and CuTA@MnO_2 samples. J) Zeta potential for MnO_2, TA@MnO_2, and CuTA@MnO_2 samples via DLS. K) XPS spectra for CuTA@MnO_2.

peak around 525 cm^{-1} attributed to the Mn–O vibration and the peak at 3380 cm^{-1} indicating the presence of CuTA [21].

Dynamic light scattering (DLS) measurements showed that the modification with TA decreased the Zeta potential of MnO_2 nanoflakes from −14.4 to −27.3 mV, while the incorporation of Cu increased the Zeta potential of TA@MnO_2 to −3.2 mV (Fig. 1J). The XPS pattern of CuTA@MnO_2 nanoflakes displayed characteristic peaks for C 1s, N 1s, O 1s, Mn 2p, and Cu 2p (Fig. 1K). Higher XPS resolution analysis indicated the presence of Mn $2p_{1/2}$ at 652.6 eV and Mn $2p_{3/2}$ at 641.3 eV, resulting from spin-orbit coupling in MnO_2 (Fig. S1A, Supplemental Information). The peaks of Cu 2p at 954.1 eV and 734.2 eV were attributed to Cu−O ($2p_{1/2}$) and Cu−O ($2p_{3/2}$) bond, respectively, suggesting that Cu was coordinated with the -OH in CuTA@MnO_2 (Fig. S1B, Supplemental Information). The H 1s spectrum was deconvoluted into two peaks corresponding to the bond energy of H at approximately 398.9 eV (Fig. S1C, Supplemental Information). The high-resolution XPS pattern of O 1s further confirmed the existence of C-O and Cu-O bonds (Fig. S1D, Supplemental Information). Collectively, these results confirm the successful synthesis of CuTA@MnO_2 nanoflakes.

2.2. Photothermal behaviors of CuTA@MnO_2 nanoflakes

The photothermal effect of CuTA@MnO_2 nanoflakes was assessed under NIR illumination. Thermal imaging and temperature measurements revealed significant temperature increases in both MnO_2 and CuTA@MnO_2 nanoflakes during NIR illumination, with the latter showing a more rapid heating and reaching higher temperatures compared to the control group (Fig. 2A and B). Notably, the CuTA@MnO_2 group exceeded 50 °C, likely due to the photothermal effect of Cu^{2+} [22].

We also examined the temperature changes of CuTA@MnO_2 nanoflakes under varying NIR power intensities (Fig. 2C). The results showed that the heating rate significantly increased as power intensity rose. Remarkably, CuTA@MnO_2 nanoflakes reached 60 °C after just 200 s of illumination at a power intensity of 2 W/cm^2, indicating a strong photothermal effect. Furthermore, as the concentration of CuTA@MnO_2 nanoflakes elevated from 0.5 to 1.5 mg/mL, the temperature rose proportionally, suggesting a concentration-dependent effect (Fig. 2D).

To evaluate the photothermal stability, the temperature of the CuTA@MnO_2 nanoflakes returned to baseline within 10 min after NIR illumination ceased (Fig. 2E). Additionally, the temperature profiles remained consistent even after 10 cycles of NIR illumination and pause (Fig. 2F). These findings demonstrate that CuTA@MnO_2 nanoflakes exhibit stable and controllable photothermal behavior.

2.3. Antibacterial performance of CuTA@MnO_2 nanoflakes

The antibacterial performance of CuTA@MnO_2 nanoflakes was evaluated against two typical Escherichia coli (E. *coli*) and methicillin-resistant staphylococcus aureus (MRSA) bacteria [23]. Live & dead staining revealed that MRSA cells were viable in MnO_2 and CuTA@MnO_2 nanoflakes without NIR illumination. However, after NIR

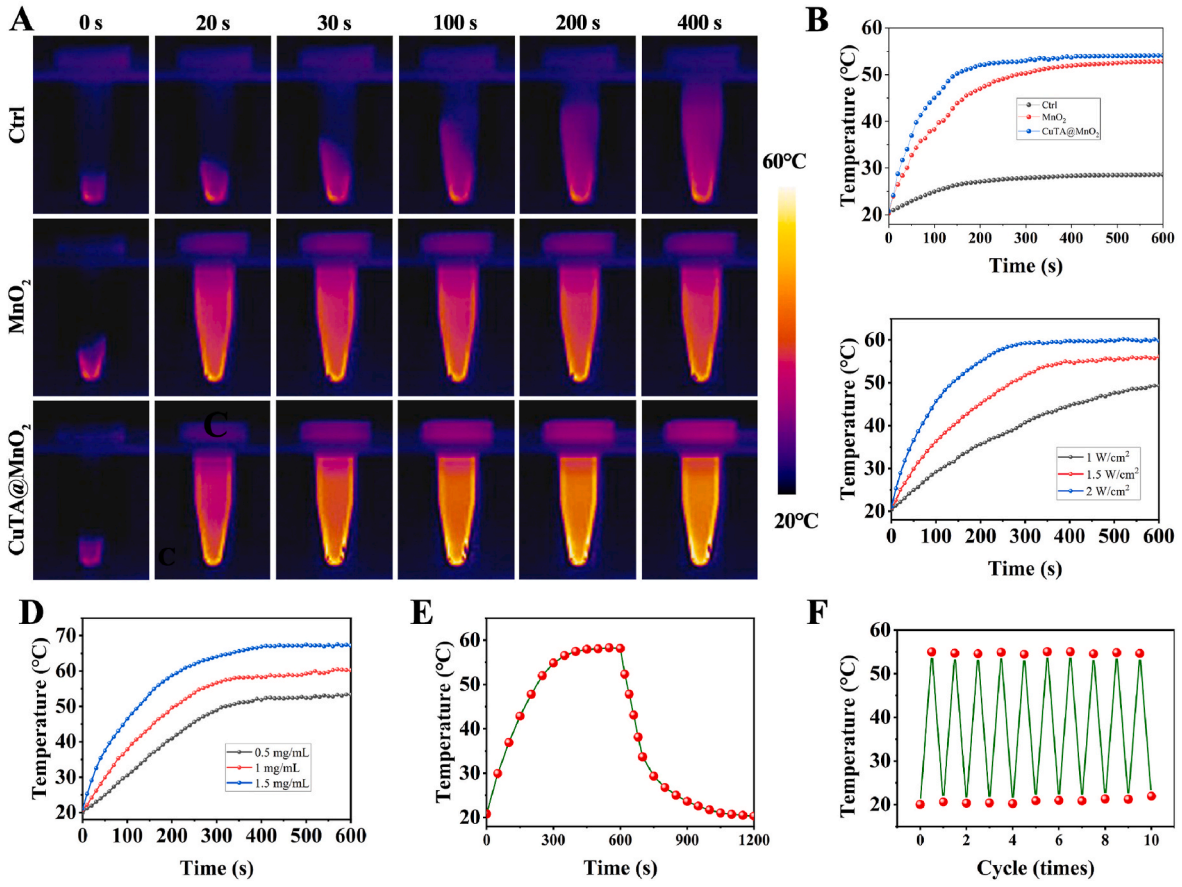

Fig. 2. Optothermal behaviors of CuTA@MnO_2 nanoflake. A) Thermal images and B) temperature profiles illustrating temperature changes in Ctrl, MnO_2, and CuTA@MnO_2 groups in a concentration of 1 mg/mL upon NIR illumination (1.5 W/cm^2). C) Temperature profiles illustrating temperature changes in CuTA@MnO_2 group in a concentration of 1 mg/mL with different power intensity (1, 1.5, and 2 W/cm^2). D) Temperature profiles illustrating temperature changes in CuTA@MnO_2 group upon NIR illumination (1.5 W/cm^2) with different nanoflake concentrations (0.5, 1, and 1.5 mg/mL). E) Time-temperature curve in CuTA@MnO_2 group (Concentration: 1 mg/mL) upon 10 min NIR illumination (1.5 W/cm^2) and cool-off for another 10 min. F) Recycling heating-cooling curves in CuTA@MnO_2 group (Concentration: 1 mg/mL) for 10 repeated NIR illumination (1.5 W/cm^2).

illumination, a considerable number of MRSA cells were dead in MnO_2 and CuTA@MnO_2 nanoflakes, while MRSA cells remained viable in the control (Ctrl) group under the same conditions (Fig. 3A). SEM observation further collaborated crumpled morphologies of both E. *coli* and MRSA in MnO_2 and CuTA@MnO_2 nanoflakes after NIR illumination, whereas these bacterial in Ctrl, and MnO_2 and CuTA@MnO_2 nanoflakes without NIR illumination keep favorable intact (Fig. S2, Supplemental Information). Quantification of bacterial cell viability showed significantly lower levels in the MnO_2 and CuTA@MnO_2 groups upon NIR illumination compared to their respective non-irradiated conditions (Fig. 3B).

Additionally, an in vitro bacteriostasis experiment was performed by the incubation of CuTA@MnO_2 nanoflakes with both E. *coli* and MRSA. Our results revealed a significantly reduced number of bacterial colonies for both E. *coli* and MRSA in the MnO_2 and CuTA@MnO_2 groups under NIR illumination, compared to those without NIR exposure (Fig. 3C). Quantification of survival rates for E. *coli* and MRSA further confirmed substantially lower levels in the MnO_2 and CuTA@MnO_2 groups with NIR illumination (Fig. 3D and E). These findings demonstrate the effective photothermal antibacterial properties of CuTA@MnO_2 nanoflakes.

2.4. Oxidation resistance of CuTA@MnO_2 nanoflakes

To assess the antioxidant capabilities of CuTA@MnO_2 nanoflakes, the clearance rates of typical ROS, including H_2O_2 and $\bullet O_2^-$, were evaluated in vitro [24]. The MnO_2 group exhibited a significantly enhanced clearance effect on H_2O_2 and $\bullet O_2^-$ compared to the Ctrl group (Fig. 4A and B). Importantly, the TA@MnO_2 and CuTA@MnO_2 groups demonstrated even greater ROS elimination capabilities, with nearly 100 % clearance of H_2O_2 and approximately 90 % clearance of $\bullet O_2^-$ after 5 h. This suggests that MnO_2 and TA synergistically enhance ROS clearance, indicating the superior antioxidant potential of CuTA@MnO_2 nanoflakes.

Further, fibroblasts pretreated with H_2O_2 to induce oxidative stress were incubated with CuTA@MnO_2 nanoflakes to detect intracellular ROS. After H_2O_2 treatment, significant red-stained dead fibroblasts were observed in control group, while fibroblasts in the MnO_2, TA@MnO_2, and CuTA@MnO_2 groups remained viable on day 3 (Fig. S3, Supplemental Information). Fluorescence imaging revealed significant ROS staining in the Ctrl group, moderate staining in the MnO_2 group, and minimal ROS fluorescence intensity in the blank, TA@MnO_2, and CuTA@MnO_2 groups (Fig. 4C). Flow cytometry data confirmed fibroblasts in the control group exhibited remarkable fluorescence intensity after H_2O_2 stimulation, indicative of oxidative stress and substantial cell damage (Fig. 4D and E). However, cells in the MnO_2 group displayed moderate fluorescence intensity, while those in the TA@MnO_2 and CuTA@MnO_2 nanoflakes exhibited negligible fluorescence intensity as compared to the blank group, indicating the inclusion of MnO_2 and TA endows mitigative effect to H_2O_2-induced oxidative stress.

Considering the overheating of CuTA@MnO_2 after NIR illumination could generate ROS [25], the ROS levels in fibroblasts were detected when incubated with CuTA@MnO_2 upon NIR illumination (Fig. S4, Supplemental Information). The results indicated negligible ROS levels in blank, MnO_2, TA@MnO_2, and CuTA@MnO_2 groups, whereas significant ROS levels in the H_2O_2-treated group (Fig. S5, Supplemental

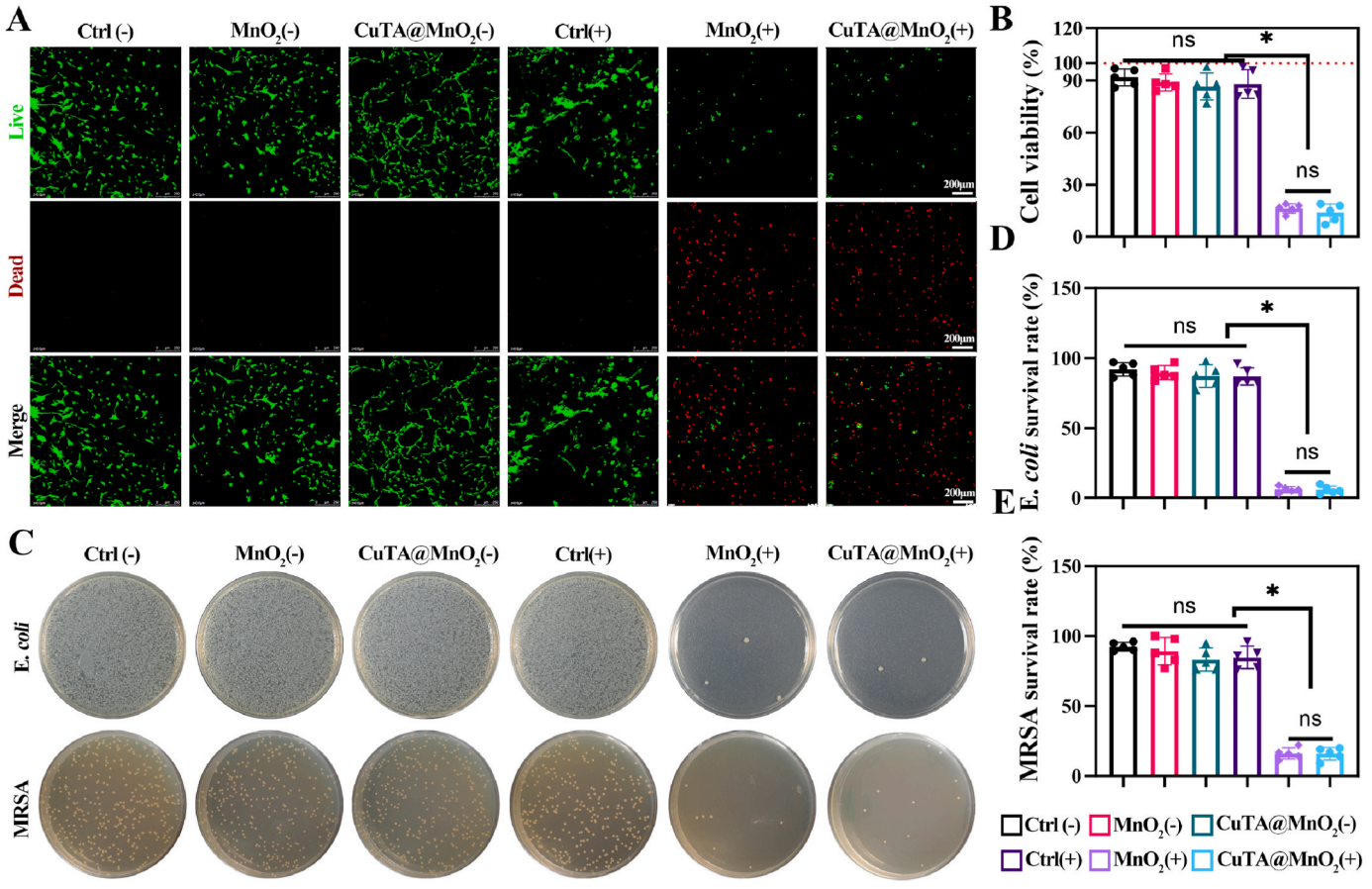

Fig. 3. Antibacterial performance of CuTA@MnO_2 upon NIR illumination. A) Live/dead staining and B) cell viability quantification of MRSA in Ctrl, MnO_2, and CuTA@MnO_2 groups in the presence or absence of NIR illumination. C) Photographs for E. *coli* and MRSA colonies in Ctrl, MnO_2, and CuTA@MnO_2 groups in the presence or absence of NIR illumination. D) E. *coli* and E) MRSA survival rates in Ctrl, MnO_2, and CuTA@MnO_2 groups in the presence or absence of NIR illumination. (−) in the of NIR illumination; (+) in the presence of NIR illumination; n = 5 per group; *$p < 0.05$; "ns" mean no statistical significance.

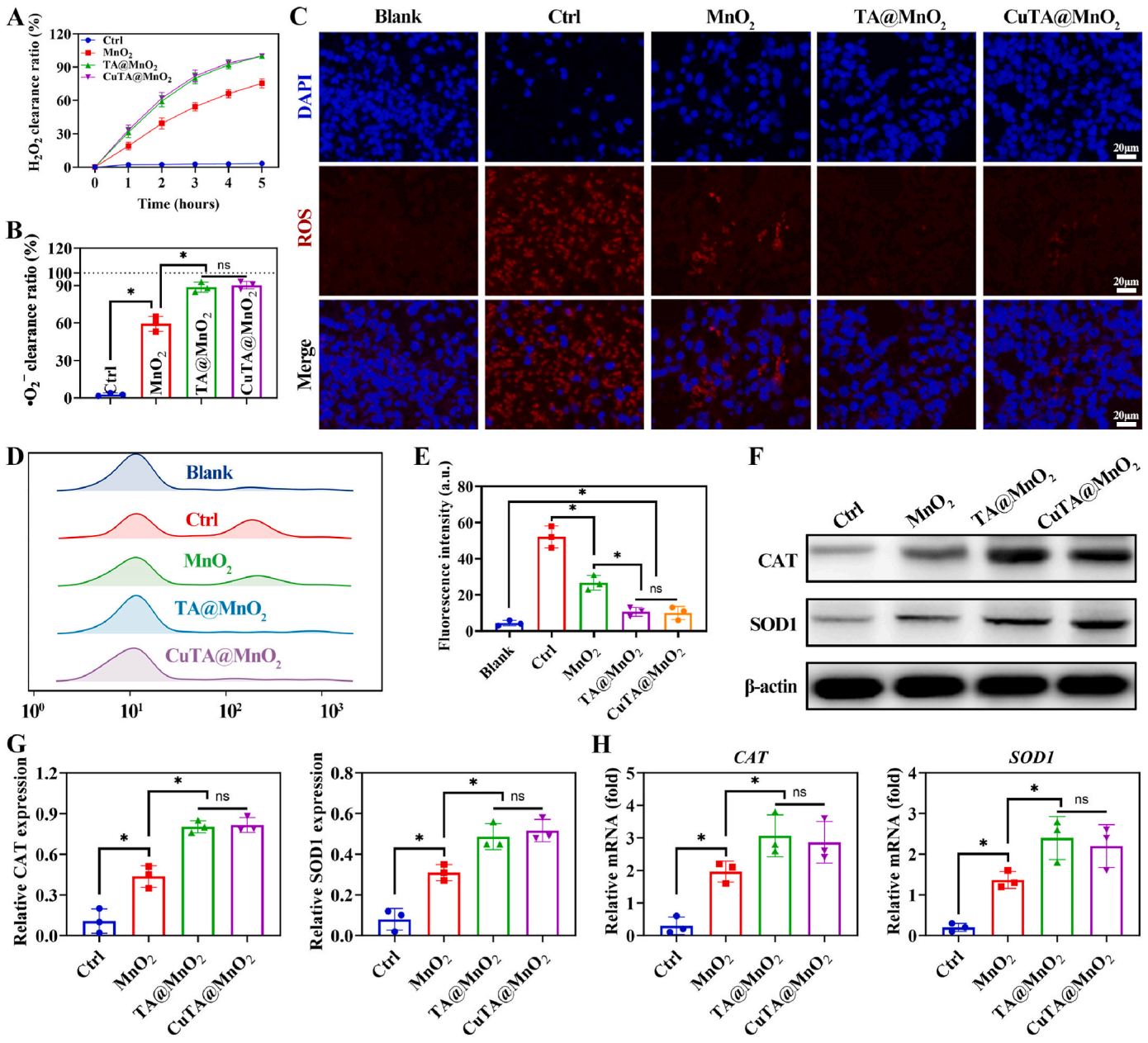

Fig. 4. Antioxidant capacities of CuTA@MnO_2 nanoflake. A) H_2O_2 and B) $\bullet O_2^-$ clearance ratio in Ctrl, MnO_2, TA@MnO_2, and CuTA@MnO_2 groups. C) Intercellular DCFH-DA staining of H_2O_2-treated fibroblast in blank, Ctrl, MnO_2, TA@MnO_2, and CuTA@MnO_2 groups. D) Fluorescence intensity and E) its quantification of fibroblasts using flow cytometry. F) Protein expression profiles of CAT and SOD1 in Ctrl, MnO_2, TA@MnO_2, and CuTA@MnO_2 groups using WB examination. G) Relative expression levels of CAT and SOD1 in Ctrl, MnO_2, TA@MnO_2, and CuTA@MnO_2 groups. H) Gene pression profiles of *CAT* and *SOD1* in Ctrl, MnO_2, TA@MnO_2, and CuTA@MnO_2 groups using RT-PCR analysis. $^*p < 0.05$; "ns" mean no statistical significance.

Information). These findings confirmed that the addition of MnO_2 and TA significantly enhances the ROS scavenging capacity of CuTA@MnO_2 nanoflakes. The low intracellular ROS levels in the MnO_2 group may also be attributed to the limited photothermal effect of MnO_2 nanoflakes, as MnO_2 scavenges ROS by catalyzing the decomposition of H_2O_2 into O_2, facilitated by redox reactions involving the Mn element in MnO_2 [26].

Moreover, live & dead staining showcased that fibroblasts in the Ctrl, MnO_2, TA@MnO_2, and CuTA@MnO_2 groups survived well upon NIR illumination, suggesting well cytocompatibility of these nanoflakes (Fig. S6, Supplemental Information). In contrast, fibroblasts in the MnO_2, TA@MnO_2, and CuTA@MnO_2 groups exhibited apparent cell death upon NIR illumination, further corroborating the strong photothermal effect of our synthesized CuTA@MnO_2 nanoflakes.

Studies have indicated that both MnO_2 and TA exert their antioxidant effects by mimicking the catalytic actions of biological enzymes [27]. In this study, western blot (WB) analysis showed higher protein levels of catalase (CAT) and superoxide dismutase 1 (SOD1) in the MnO_2 group compared to the Ctrl group (Fig. 4F and G), indicating enhanced catalytic activity. Notably, the TA@MnO_2 and CuTA@MnO_2 groups showed even higher expression levels of CAT and SOD1 proteins than the MnO_2 group, suggesting a synergistic effect of TA and MnO_2 in enhancing the catalytic actions of CuTA@MnO_2 nanoflakes. These findings were corroborated by reverse transcription-polymerase chain reaction (RT-PCR) analysis of *CAT* and *SOD1* genes expression, which aligned with the protein expression levels (Fig. 4H). Collectively, these data corroborate that CuTA@MnO_2 nanoflakes possess favorable antioxidant capabilities by exerting the catalytic actions of biological enzymes [12].

2.5. Pro-angiogenic function of CuTA@MnO_2 nanoflakes

Angiogenesis is crucial in healing IDW, which typically suffer from poor blood circulation, leading to inadequate oxygen and nutrient supply, thereby delaying the healing process [28]. Enhancing blood vessel formation can significantly accelerate wound healing by improving oxygen and nutrient delivery, promoting cell proliferation and repair, and reducing complications. Given the role of Cu^{2+} in promoting angiogenesis in CuTA@MnO_2 nanoflakes [29], we first examined the in vitro release kinetics of Cu. The results showed a significant release of Cu^{2+} under NIR illumination, compared to the absence of illumination, over 25 h of incubation in phosphate-buffered saline (PBS, Fig. S7, Supplemental Information). This suggests that the hyperthermic environment created by NIR illumination enhances Cu^{2+} release from CuTA@MnO_2 nanoflakes.

Subsequently, an in vitro angiogenesis experiment was conducted to evaluate the pro-angiogenic potential of CuTA@MnO_2 nanoflakes. Light microscopy images from the migration assay revealed significant migration of human umbilical vein endothelial cells (HUVECs) only in the CuTA@MnO_2 group under NIR illumination, compared to the control group and other nanoflake groups (MnO_2, TA@MnO_2), either with or without NIR illumination (Fig. 5A). Quantitative analysis confirmed the highest HUVEC migration levels in the CuTA@MnO_2 group post-NIR illumination (Fig. 5B). Similarly, in vitro tube formation assays showed that only CuTA@MnO_2 nanoflakes formed capillary-like structures under NIR illumination, while the other groups displayed individual cells or small clusters (Fig. 5C). Quantitative analysis of branch points and tube formation confirmed significantly higher levels in the CuTA@MnO_2 group under NIR illumination (Fig. 5D). These findings indicate that NIR-induced hyperthermia enhances Cu release, thereby promoting angiogenesis.

To further investigate the mechanisms by which released Cu promotes angiogenesis, we analyzed the gene and protein expression profiles of nanoflake-treated HUVECs under NIR illumination. Our data showed that the expression levels of angiogenesis-related genes, including *VEGF*, platelet derived growth factor (*PDGF*), and hypoxia inducible factor-1α (*HIF-1α*), were markedly elevated in the CuTA@MnO_2 group compared to the control, MnO_2, and TA@MnO_2 groups (Fig. 5E). Protein expression levels corroborated these findings (Fig. 5F), suggesting that Cu released from CuTA@MnO_2 nanoflakes promotes angiogenesis by upregulating VEGF, PDGF, and HIF-1α expression.

2.6. Characterization of CuTA@MnO_2 microneedles

Inspired by the favorable antibacterial, antioxidant, and pro-

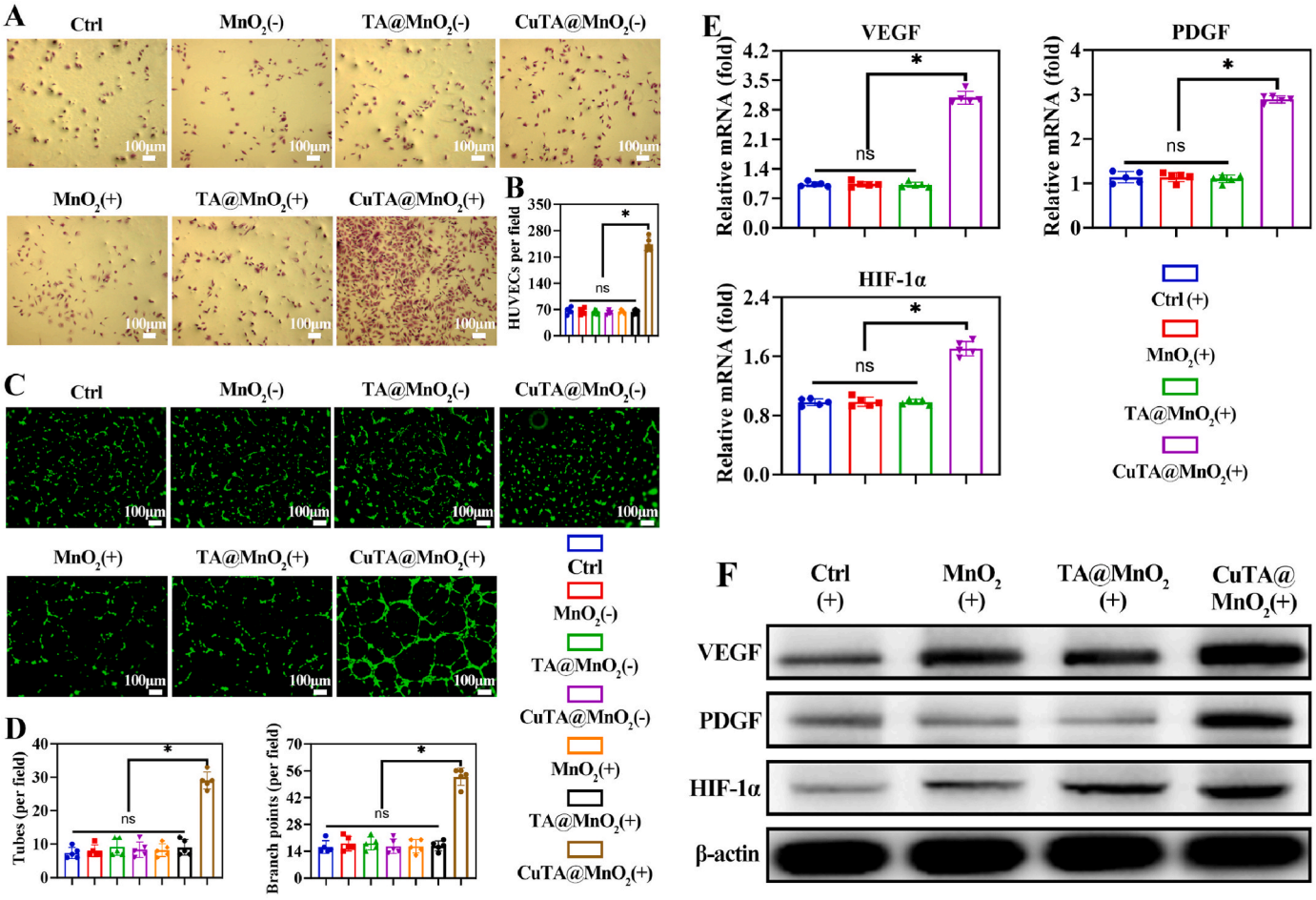

Fig. 5. Angiogenic effect of CuTA@MnO_2 nanoflake upon NIR illumination. A) Light microscope and B) its corresponding quantification for migrated HUVECs stained with crystal violet using a Transwell assay in Ctrl, MnO_2, TA@MnO_2, and CuTA@MnO_2 groups in the presence or absence of NIR illumination. C) Fluorescence microscope and D) its corresponding quantifications (Tubes per and branch points per filed) for tube formation in Ctrl, MnO_2, TA@MnO_2, and CuTA@MnO_2 groups in the presence or absence of NIR illumination. E) Relative mRNA expression (*VEGF*, *PDGF*, and *HIF-1α*) of HUVECs in Ctrl, MnO_2, TA@MnO_2, and CuTA@MnO_2 groups upon NIR illumination using RT-PCR analysis. F) Relative protein expression (VEGF, PDGF, and HIF-1α) of HUVECs in Ctrl, MnO_2, TA@MnO_2, and CuTA@MnO_2 groups upon NIR illumination using WB examination. (−) in the absence of NIR illumination; (+) in the presence of NIR illumination; n = 5 per group; *$p < 0.05$; "ns" mean no statistical significance.

angiogenic properties, CuTA@MnO_2 nanoflakes were further mixed with a methacrylated HA solution to develop CuTA@MnO_2 microneedle (Fig. S8, Supplemental Information). Photographs revealed that the CuTA@MnO_2 microneedles exhibited multiple regularly arranged tips on a pedestal (Fig. 6A). Light microscopy images clearly showed cone-shaped tips with an approximate radius of 120 μm and a height of around 300 μm (Fig. 6B–D). The SEM images showed that the height of the microneedle tips is 298.56 ± 4.54 μm, the radius of the cone-shaped tips is 120.47 ± 3.62 μm, and the spacing between the microneedle tips is 125.62 ± 4.53 μm, with a dispersion coefficient of 3.6 %, which corroborates the observations made with light microscopy. Additionally, the SEM images of the synthesized CuTA@MnO_2 microneedles reveal a homogeneous and transparent microneedle structure with no visible aggregation, indicating an even distribution of CuTA@MnO_2 within the HA matrix (Fig. 6E–G).

To verify whether the synthesized CuTA@MnO_2 microneedles retained their photothermal effect, they were exposed to NIR illumination. Thermal images demonstrated a significant temperature increase in both MnO_2 and CuTA@MnO_2 microneedles after 400 s of NIR illumination (Fig. 6H). The CuTA@MnO_2 microneedles showed superior temperature elevation, indicating that CuTA modification enhances the photothermal effect. Quantification confirmed a marked temperature rise in both MnO_2 and CuTA@MnO_2 microneedles, with the latter exceeding 50 °C within 600 s (Fig. 6I). Additionally, the temperature increase in CuTA@MnO_2 microneedles was power intensity- and concentration-dependent (Figs. S9A–B, Supplemental Information), further demonstrating their excellent photothermal performance.

The in vitro degradation rate of CuTA@MnO_2 microneedles was also evaluated after immersion in PBS. The results showed complete degradation within 7 days under NIR illumination, compared to 13 days without illumination (Fig. S10, Supplemental Information), indicating that NIR illumination accelerates microneedle degradation. The spontaneous degradation under NIR illumination is driven by various physical, chemical, and biological mechanisms. CuTA@MnO_2, with its high light absorption and photothermal conversion efficiency in the NIR range, rapidly increases the local temperature of the microneedles, causing softening and accelerated degradation, facilitating drug release in a controlled manner.

Mechanical strength is critical for microneedles to penetrate IDW tissue and deliver drugs [30]. Compression-strain curves demonstrated a

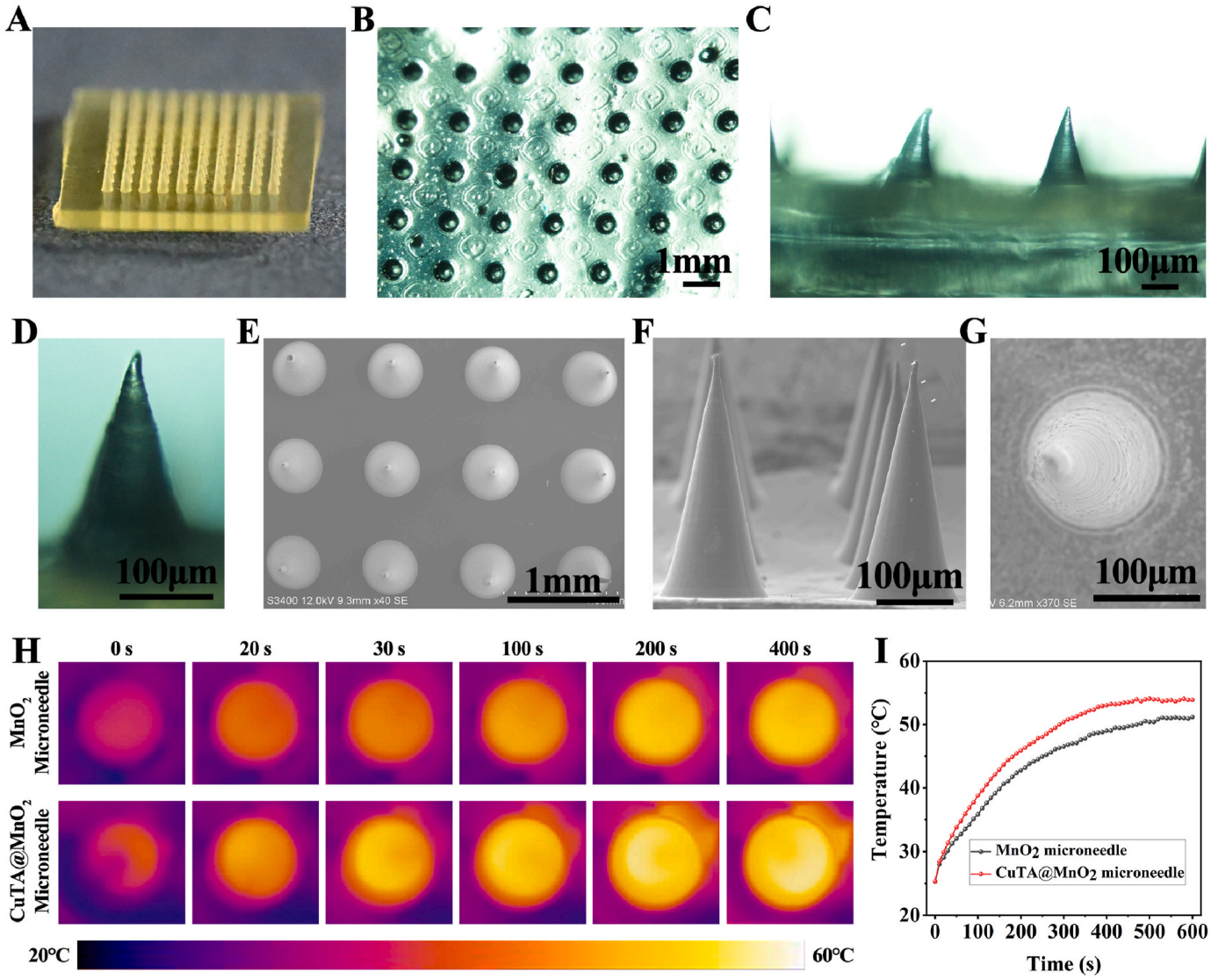

Fig. 6. Synthesis and optothermal behaviors of CuTA@MnO_2 microneedle. A) Photographs for fabricated CuTA@MnO_2 microneedle. B-D) Light microscope of CuTA@MnO_2 microneedle. E-G) SEM images of CuTA@MnO_2 microneedle. H) Thermal images of MnO_2 and CuTA@MnO_2 microneedles in a concentration of 1 mg/mL upon NIR illumination (1.5 W/cm^2). J) Temperature profiles in MnO_2 and CuTA@MnO_2 microneedles with varying time (0–600 s) in a concentration of 1 mg/mL upon NIR illumination (1.5 W/cm^2).

gradual increase in compressive force with increased strain (Fig. S11A, Supplemental Information), indicating that the CuTA@MnO_2 microneedles keep intact under compressive test. Hematoxylin-eosin (HE) staining confirmed successful insertion into rat IDW tissue, with multiple cavities resembling the cone-shaped tips observed near the muscle layer (Fig. S11B, Supplemental Information).

For effective IDW treatment, the release of therapeutic agents following microneedle insertion is essential. CuTA@MnO_2 microneedles, labeled with fluorescein isothiocyanate (FITC), were inserted into IDW tissue, showing increased FITC intensities from 5 to 120 min (Fig. S12, Supplemental Information). This suggests gradual microneedle degradation, releasing Cu, MnO_2, and TA. The methacrylated HA used in our microneedles is biocompatible and biodegradable, which minimizes the risk of adverse reactions or interference with the wound healing process. Additionally, the microneedles are designed to create minimal trauma, reducing the likelihood of complications such as infection. The voids left by the microneedles are small and temporary, as the microneedles degrade over time, allowing the skin to heal naturally. Collectively, these findings indicate that CuTA@MnO_2 microneedles are minimally invasive, capable of penetrating deep into rat IDW tissue to deliver drugs through the physiological barrier and gradually degrading to release therapeutic agents.

Before biological applications, biosafety assessments are crucial [31]. Pure microneedles, MnO_2 microneedles, TA@MnO_2 microneedles, and CuTA@MnO_2 microneedles were separately inserted into the skin of rats for 21 days. Histological examination using HE staining revealed no

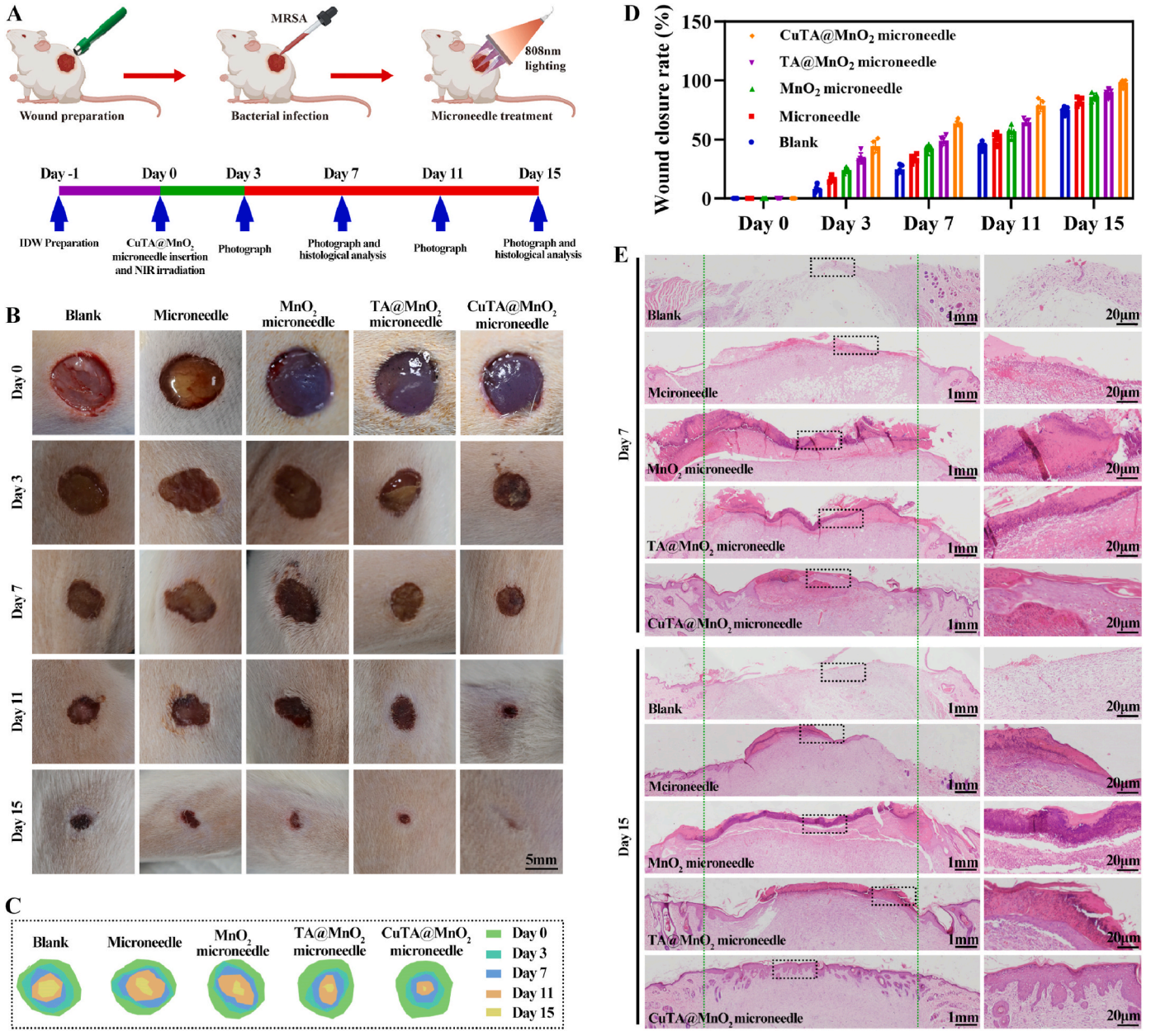

Fig. 7. Therapeutic outcome of CuTA@MnO_2 microneedle for IDW in a rat model. A) Flow diagram for the treatment of CuTA@MnO_2 microneedle in a rat IDW model. B) Photograph for repaired wound in blank, microneedle, MnO_2 microneedle, TA@MnO_2 microneedle, and CuTA@MnO_2 microneedle at 0, 3, 7, 11, and 15 days. C) Trajectory diagram for the IDW healing progress in various groups. D) Quantification of wound closure rate in blank, microneedle, MnO_2 microneedle, TA@MnO_2 microneedle, and CuTA@MnO_2 microneedle. E) HE staining for repaired wounds in blank, microneedle, MnO_2 microneedle, TA@MnO_2 microneedle, and CuTA@MnO_2 microneedle, in which the right panels are the magnified images of the left panels. The green dotted lines outline the border between normal skin and repaired wound.

noticeable organ damage in the heart, liver, spleen, lungs, or kidneys in any group (Fig. S13, Supplemental Information). No animal deaths or abnormal behavior were observed, indicating that CuTA@MnO_2 microneedles are biocompatible and safe, showcasing their potential as drug-delivery platforms for IDW treatment.

2.7. IDW healing efficiency of CuTA@MnO_2 microneedles

To assess the effectiveness of CuTA@MnO_2 microneedle in accelerating IDW healing, an IDW model was established in Sprague Dawley rats by inducing diabetes with a high-sugar diet followed by MRSA injection. The experimental setup for the animal study is depicted in Fig. 7A. Photographic images and wound healing trajectory plots showcased progressive wound healing in all five groups over 15 days post-treatment (Fig. 7B and C). Quantitative analysis of scar length suggested the shortest scars in CuTA@MnO_2 group at both 7 and 15 days in comparison to other four groups (Fig. S14A, Supplemental Information). Notably, the CuTA@MnO_2 microneedle-treated wounds were almost completely healed by day 15, whereas the other groups required more time for complete healing (Fig. S14B, Supplemental Information), highlighting the superior healing capacity of the CuTA@MnO_2 microneedles. The wound closure rate further confirmed a significant reduction in wound areas in all microneedle-treated groups, particularly in the CuTA@MnO_2 microneedle group (Fig. 7D).

Histological examination using HE dye indicated that the CuTA@MnO_2 microneedle group displayed faster wound closure and re-epithelialization in comparison to the other four groups on day 7. By day 15, the CuTA@MnO_2 group showed complete re-epithelialization, while other groups only demonstrated partial wound closure and re-epithelialization (Fig. 7E). These results suggest that CuTA@MnO_2 microneedles are highly effective in promoting IDW healing.

Bacterial presence is significant barrier to IDW healing [32]. Fluorescence in situ hybridization (FISH) staining and corresponding bacterial intensity data revealed higher bacterial levels in the blank, pure microneedle, and MnO_2 microneedle groups at both 7 and 15 days, while the TA@MnO_2 microneedle group showed lower bacterial levels,

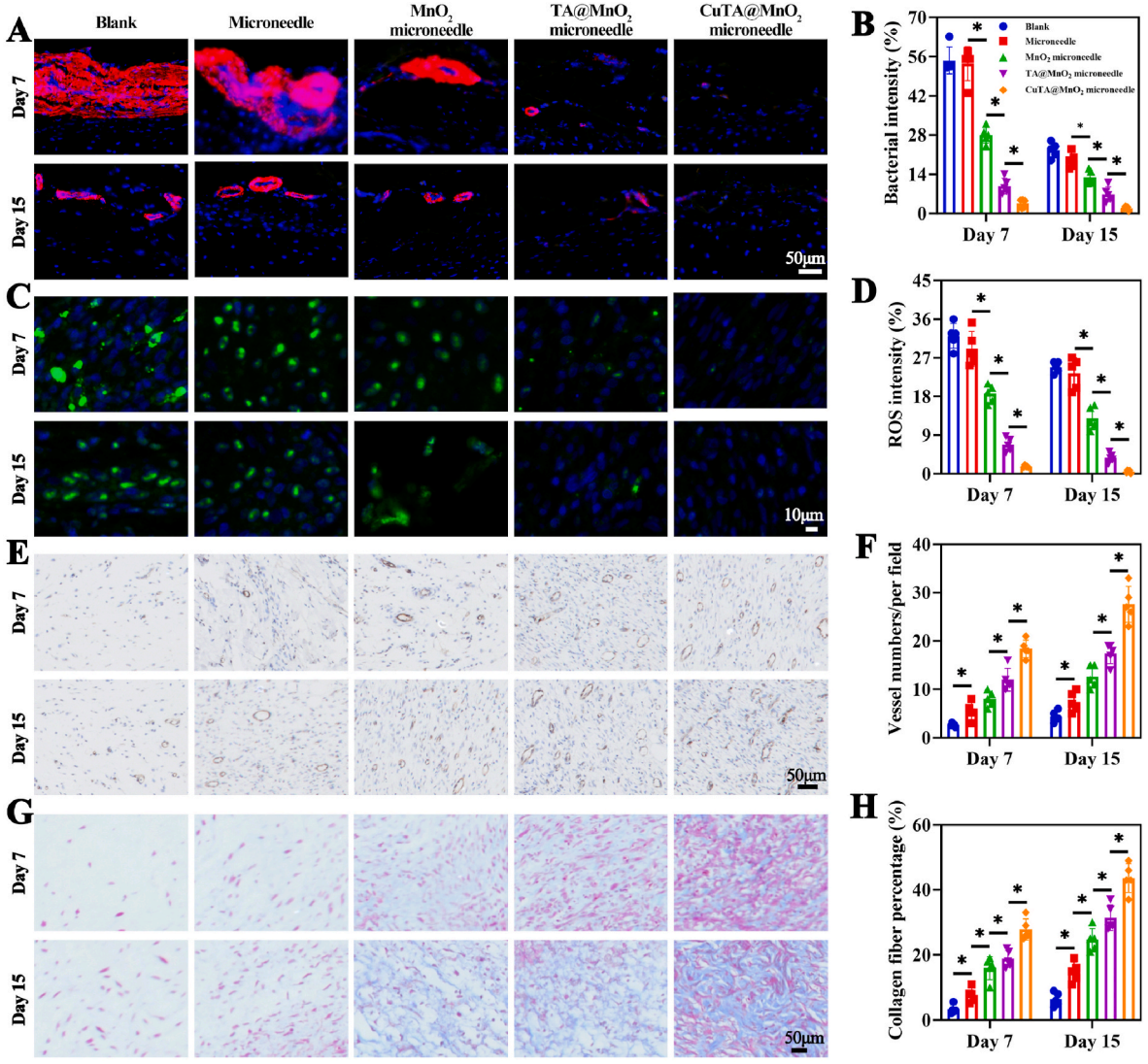

Fig. 8. Evaluations of antibacterial, antioxidant, angiogenic, and collagen deposition for the repaired wound tissue in various groups. A) FISH staining and B) its corresponding quantification for bacterial intensity in blank, microneedle, MnO_2 microneedle, TA@MnO_2 microneedle, and CuTA@MnO_2 microneedle at day 7 and 15. C) ROS immunofluorescence staining and D) its corresponding quantification for ROS intensity in blank, microneedle, MnO_2 microneedle, TA@MnO_2 microneedle, and CuTA@MnO_2 microneedle at day 7 and 15. E) CD31 immunohistochemical staining and F) its corresponding quantification for vessel numbers per field in blank, microneedle, MnO_2 microneedle, TA@MnO_2 microneedle, and CuTA@MnO_2 microneedle at day 7 and 15. G) Masson's Trichrome staining and H) its corresponding quantification for collagen fiber percentage in blank, microneedle, MnO_2 microneedle, TA@MnO_2 microneedle, and CuTA@MnO_2 microneedle at day 7 and 15. *$p < 0.05$.

and the CuTA@MnO_2 microneedle group exhibited almost no bacterial presence (Fig. 8A and B). These findings underscore the satisfactory bacterial combating behavior of CuTA@MnO_2 microneedles under NIR illumination, largely due to their effective photothermal properties [33]. Immunofluorescence ROS staining and intensity data also demonstrated the lowest levels of ROS in the CuTA@MnO_2 microneedle group in comparison to other four groups on days 7 and 15 (Fig. 8C and D), indicating the superior antioxidant properties of CuTA@MnO_2 microneedles.

Moreover, the CuTA@MnO_2 microneedles exhibited the strongest pro-angiogenic ability, as evidenced by the most intense CD31 marker staining in immunohistochemical analyses (Fig. 8E) and the highest number of vessels per field (Fig. 8F) over 7–15 days. Masson's trichrome staining and quantitative analysis of total collagen fiber percentage further demonstrated that the CuTA@MnO_2 microneedle possessed optimal collagen formation in comparison to other four groups over

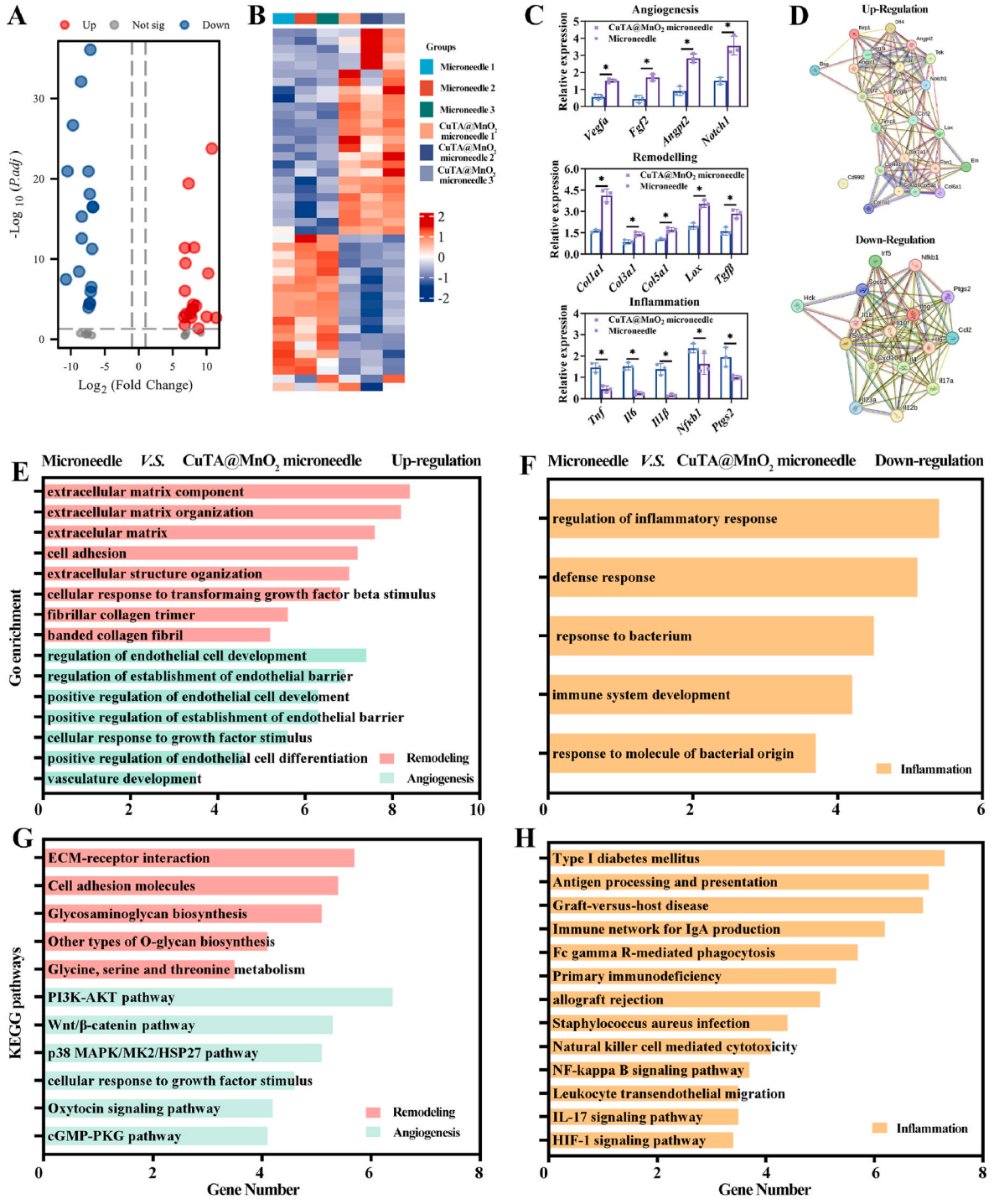

Fig. 9. Whole transcriptome RNA sequencing for the repaired wound tissue. A) Volcano plot and B) heatmap of upregulated and downregulated genes in the repaired wound tissue after microneedle and CuTA@MnO_2 microneedle treatment. C) Relative expression of genes related to angiogenesis, inflammation, and remodeling in the repaired wound tissue after microneedle and CuTA@MnO_2 microneedle treatment. D) String diagram of gene–gene interactions in up-regulated and down-regulated genes. GO enrichment analysis of the E) up-regulated and F) down-regulated genes related to angiogenesis, inflammation, and remodeling. KEGG pathway enrichment analysis of the G) up-regulated and H) down-regulated genes related to angiogenesis, inflammation, and remodeling.

7–15 days (Fig. 8G and H). Immunohistochemical staining for collagen I and III, along with their corresponding intensity measurements, supported these findings (Fig. S15, Supplemental Information).

Collectively, these in vivo results demonstrate that CuTA@MnO_2 microneedles excel in bacterial elimination, ROS scavenging, and promoting angiogenesis. These favorable factors contribute to wound healing, epithelialization, and collagen regeneration, making CuTA@MnO_2 microneedles high-efficiency in expediting IDW rehabilitation.

2.8. Transcriptome RNA sequencing for the repaired wound tissue

At day 15, whole RNA sequencing was conducted on repaired wound tissues to delve deeper into the mechanism by which CuTA@MnO_2 microneedles facilitate IDW healing. To emphasize the biological role of CuTA@MnO_2 microneedle, pore microneedle was served as the control group in this study. The resulting volcano plot indicated 19 genes down-regulated and 26 genes up-regulated (Fig. 9A). Differential analysis of gene expression profiles between the pure microneedle and CuTA@MnO_2 microneedle revealed significant differences (Fig. 9B and Figs. S16A–C, Supplemental I**nformation**).

An enrichment analysis, based on the differentially expressed genes, highlighted distinctive gene expression patterns in the wound tissues of the pure microneedle and CuTA@MnO_2 microneedle (Fig. 9C). Specifically, genes associated with angiogenesis (e.g., *vegfa, fgf2, angpt2, notch1,* etc.) and remodeling (e.g., *col1a1, col3a1, col5a1, lox, tgfβ,* etc.) exhibited upregulation in the CuTA@MnO_2 microneedle compared to the pure microneedle. Conversely, genes linked to inflammation (e.g., *tnf, il6, il1β, nfκb1, ptgs2*, etc.) showed significant downregulation in the CuTA@MnO_2 microneedle. Gene string diagrams and protein interactions supported the close interconnection between these processes (Fig. 9D).

Further gene ontology (GO) analysis unveiled enrichment of upregulated genes in angiogenesis and remodeling in the CuTA@MnO_2 microneedle, while downregulated genes were associated with inflammatory clusters (Fig. 9E and F). These biological processes were underscored by the regulation of extracellular matrix organization, collagen deposition, vasculature development, and inflammatory factors. Kyoto Encyclopedia of Genes and Genomes (KEGG) pathway analysis indicated activation of ECM-receptor interaction, glycosaminoglycan biosynthesis, PI3K-AKT, Wnt/β-catenin, and oxytocin signaling pathways in the CuTA@MnO_2 microneedle (Fig. 9G). These pathways bolstered collagen remodeling and angiogenesis while suppressing pathways linked to inflammation such as allograft rejection, natural killer cell-mediated cytotoxicity, NF-κB, and HIF-1 signaling (Fig. 9H). Overall, transcriptome RNA sequencing data demonstrated that CuTA@MnO_2 microneedle positively regulate wound tissue by promoting collagen remodeling and angiogenesis while concurrently suppressing inflammation. This mechanism significantly accelerates IDW healing.

3. Conclusion

The current work synthesized a new CuTA@MnO_2 microneedle by integrating a metal-phenolic nanozyme–CuTA@MnO_2 nanoflakes–into a methacrylated HA. The multifunctional microneedle facilitated the transdermal penetration of CuTA@MnO_2 into the dermis. The photothermal behavior of CuTA@MnO_2 effectively eradicated bacteria upon exposure to NIR illumination. In addition, the hyperthermia accelerated the release of MnO_2, TA, and Cu from the CuTA@MnO_2 microneedle. As an inorganic nanoenzyme, MnO_2 could then coordinate with TA to significantly contribute to scavenging ROS at the wound site. The later released Cu^{2+} showcased pro-angiogenic effect. These chronologically orchestrated effects expedited IDW rehabilitation with accelerated wound healing, enhanced epithelialization, and increased collagen regeneration. Transcriptome RNA sequencing further supported the efficacy of the CuTA@MnO_2 microneedle in promoting collagen remodeling and angiogenesis while suppressing inflammation in the repaired wound tissue. This novel approach laying the foundation for developing a photothermal-controlled microneedle for the transdermal delivery of metal-phenolic nanozymes with staged antibacterial, antioxidant, and angiogenic effects–essential elements for effective IDW treatment.

4. Materials and methods

Preparation of CuTA@MnO_2 Nanoflakes: To synthesize CuTA nanoparticles, 27 mg of TA (Aladdin, China) and 0.9 g of $CuSO_4{\cdot}5H_2O$ (Sigma, USA) were mixed in 50 mL of de-ionized water (DI water, pH = 7.4). The solution was heated to 50 °C and maintained for 4 h, yielding the CuTA nanoparticle solution.

For MnO_2 nanoflakes synthesis, 30 mL of 0.1 M sodium dodecyl sulfate (Sigma, USA) and 1.5 mL of 0.1 M sulfuric acid (H_2SO_4, Sigma, USA) were mixed in 265.5 mL of DI water, and the solution was constantly stirred at 100 °C. Next, 3 mL of 50 mM potassium permanganate ($KMnO_4$, Sigma, USA) was added, and heating continued for an additional hour. The resulting suspension was washed multiple times with ultrapure water and absolute alcohol to obtain purified MnO_2 nanoflakes.

For polymerization, MnO_2 nanoflakes were added to an aqueous solution of Tris (2-amino-2-hydroxymethylpropane-1,3-diol) at a concentration of 20 mg/mL. The CuTA solution was then added in a 1:1 vol ratio. The mixture was stirred magnetically at 37 °C for 12 h to produce CuTA@MnO_2 nanoflakes.

Verification of CuTA@MnO_2 Nanoflakes: SEM (Hitachi, TM-1000, Japan) was used to observe the morphology of CuTA nanoparticles. TEM (DB500, CIQTEK, China) was used to observe the morphology of MnO_2 and CuTA@MnO_2 nanoflakes. The elemental composition of CuTA@MnO_2 nanoflakes was identified during TEM observation. XRD (Empyrean, Panaco, Netherlands) determined the crystal structure of CuTA nanoparticles. FTIR (F950, FAVOURITE, Tianjin, China) and XPS (VersaProbe 4, dezisemi, Shanghai, China) were used to analyze the chemical structure of the CuTA nanoparticles and CuTA@MnO_2 nanoflakes. Higher XPS resolutions were obtained to ascertain the Mn, Cu, H, and O elements. The surface zeta potential of MnO_2, CuTA@MnO_2, and CuTA@MnO_2 nanoflakes was measured using DLS (Nicomp N3000, Stawell, Beijing, China).

Photothermal Behavior of CuTA@MnO_2 Nanoflakes: MnO_2 and CuTA@MnO_2 nanoflakes (Concentration: 1 mg/mL), were separately placed in a 1.5 mL eppendorf tube, with an empty eppendorf tube serving as the Ctrl group. These samples were irradiated for 10 min using an 808 nm NIR laser at a power density of 1.5 W/cm^2, with temperature changes recorded using a thermal imaging camera. The CuTA@MnO_2 nanoflakes were then cooled to room temperature, and the heating-cooling process was repeated for 10 cycles to obtain heating-cooling curves. Additionally, temperature changes of CuTA@MnO_2 nanoflakes were recorded at varying NIR power densities (1 W/cm^2, 1.5 W/cm^2, and 2 W/cm^2) with a 1 mg/mL concentration, and at different concentrations (0.5 mg/mL, 1 mg/mL, and 1.5 mg/mL) with a constant NIR density of 1.5 W/cm^2.

Antibacterial Performance of CuTA@MnO_2 Nanoflakes: Both the bacteria of E. *coli* and MRSA were suspended to a density of 1×10^9 colony-forming units (CFU)/mL. Then, 400 mL of both suspensions were separately cocultured with PBS (Ctrl), MnO_2, and CuTA@MnO_2 nanoflakes, and treated with or without NIR illumination for 10 min. The parameters for NIR illumination are 808 nm in wave length, and 1.5 W/cm^2 of power densities, and lasted for 10 min, and were also applied to for all the following experiments in this study unless otherwise stated. The solutions were then cultured on Luria-Bertani agar plates for 24 h, and bacterial survival of both E. *coli* and MRSA was grossly observed and quantified. The morphological changes of both E. *coli* and MRSA were also observed via a SEM examination.

Additionally, MRSA cells in all the Ctrl, MnO_2, and CuTA@MnO_2 groups the with and without NIR illumination were subjected to a Live & Dead Bacterial Staining Kit (Yeasen, China) and observed under a fluorescence microscope (Leica, Germany). The bacterial cell viability was determined from the obtained images via an ImageJ software.

Antioxidation Behavior of CuTA@MnO_2 Nanoflakes: MnO_2, TA@MnO_2, and CuTA@MnO_2 nanoflakes, along with 10 μL PBS (Ctrl group), were incubated separately with H_2O_2 (10 Mm, 50 μL) at 37 °C for 5 h. The supernatants were then dissolved in 10 μL of 5 mM $Ti(SO_4)_2$ supplemented with 3 M H_2SO_4 for 10 min. Pure PBS without H_2O_2 served as the blank sample. Absorbance values were recorded every hour from 0 to 5 h at 405 nm and used to calculate the H_2O_2 clearance ratio as previous reported method [34].

The O_2^- clearance ratio in Ctrl group, as well as MnO_2, TA@MnO_2, and CuTA@MnO_2 nanoflake groups were determined via a Superoxide Anion Assay Kit (KMS02315, KEMOBio, China).

L929 fibroblasts, purchased from Gaide Chemical Network (China), were pre-treated with 100 μM H_2O_2 and incubated with MnO_2, TA@MnO_2, and CuTA@MnO_2 nanoflakes for 3 days. Fibroblasts without nanoflake treatment served as the Ctrl group, while those cultured in pure medium without H_2O_2 or nanoflakes were the blank group. All groups were subjected to a live & dead cell staining kit (Yeasen, China) and observed via fluorescence microscopy. In addition, fibroblasts without H_2O_2-treatment in Ctrl, MnO_2, TA@MnO_2, and CuTA@MnO_2 groups, and in presence or absence of NIR illumination were also subjected to this live & dead cell staining kit.

ROS levels in fibroblasts were detected using 2′,7′-Dichlorodihydrofluorescein diacetate (DCFH-DA)/4,6-diamino-2-phenyl indole (DAPI) staining. DCFH-DA was dissolved in dimethyl sulfoxide to a final concentration of 10 μM. After removing the cell culture medium and washing the cells with PBS, DCFH-DA working solution was added, and the cells were incubated at 37 °C for 30 min, avoiding light exposure. After incubation, the DCFH-DA working solution was removed, and the fibroblasts were then stained with DAPI working solution at 25 °C for 5–10 min. After washing, the fibroblasts were observed using a fluorescence microscopy. The DAPI-stained nuclei emitted blue fluorescence, while the DCFH-DA stained ROS emitted red fluorescence. Additionally, DCFH-DA labeled cells were digested with trypsin and analyzed via flow cytometry (CytoFLEX, China) to detect fluorescence intensity.

Fibroblasts were also incubated with MnO_2, TA@MnO_2, and CuTA@MnO_2 nanoflakes for 12 h, and then illuminated by NIR laser for 10 min. Fibroblasts only exposed to NIR illumination regarded as a blank group, while those treated only with H_2O_2 regarded as a ctrl group. ROS levels were detected using the method described above.

For WB analysis, proteins from H_2O_2-treated fibroblasts in Ctrl, MnO_2, TA@MnO_2, and CuTA@MnO_2 groups were isolated using a Protein Extraction Kit (Beyotime, Jiangsu, China). Protein concentration was measured using the Pierce™ BCA Protein Assay Reagent Kit (Thermo Fisher Scientific, China). Equal amounts of total protein (80 μg/lane) were resolved on 5–10 % SDS-PAGE gels and transferred onto polyvinylidene difluoride membranes. The membranes were blocked with 5 % nonfat dry milk in PBST (PBS containing 0.05 % Tween 20) and incubated overnight at 4 °C with primary antibodies against CAT and SOD1. Blots were developed using an enhanced chemiluminescence detection kit (Millipore) and visualized using a FluorChem E Imager (Protein-Simple, Santa Clara, USA). Densities relative to β-actin were analyzed using an ImageJ software.

RT-PCR was performed to assess the expression levels of *CAT* and *SOD1* genes. Total RNA was obtained from the cells in Ctrl, MnO_2, TA@MnO_2, and CuTA@MnO_2 groups via an RNA kit. The extracted RNA was then reverse-transcribed into cDNA using the PrimeScript RT Master Mix (TaKaRa) according to the manufacturer's instructions. Realtime PCR was conducted using a Bio-Rad RT-PCR system, with β-actin serving as the internal reference. Primer sequences for RT-PCR are listed in Table S1 (Supporting Information).

In Vitro Release Kinetics of Cu^{2+}: CuTA@MnO_2 nanoflakes were dispersed in 5 mL of PBS solution (pH 7.4) and maintained in a constant temperature shaker at 37 °C. At predetermined intervals, 1 mL samples of the release media were withdrawn and replaced with fresh PBS. The concentration of released Cu^{2+} was measured using inductively coupled plasma optical emission spectrometry (Varian, USA) [15].

Pro-Angiogenic Evaluation: The potential of MnO_2, TA@MnO_2, and CuTA@MnO_2 nanoflakes in promoting migration of HUVECs was evaluated using a Transwell migration assay. HUVECs were cultured in endothelial cell medium containing 5 % fetal bovine serum (FBS) and 1 % penicillin-streptomycin at 37 °C in a humidified incubator with 5 % CO_2. For the assay, HUVECs were harvested and resuspended in serum-free medium. A total of 2×10^4 cells in 200 μL of medium were seeded into the upper chamber of a 24-well Transwell insert with an 8 μm pore size. The lower chamber was filled with 600 μL of medium supplemented with 10 % FBS as a chemoattractant, without (Ctrl group) or with the presence of MnO_2, TA@MnO_2, and CuTA@MnO_2 (1 mg/mL) extracts (Pre-illuminated by NIR laser). After 24 h of incubation, non-migrated cells on the upper surface of the membrane were gently removed with a cotton swab. The migrated cells on the lower surface were fixed with 4 % paraformaldehyde, stained with crystal violet, and counted under a light microscope. The number of migrated cells was quantified in five random fields per insert.

To evaluate the effect of MnO_2, TA@MnO_2, and CuTA@MnO_2 nanoflakes with or without NIR illumination on capillary-like structure formation, a tube formation assay was conducted using Matrigel (Sigma, USA). Cold Matrigel (200 μL) was added to each well of a 24-well plate, followed by the addition of 200 μL of pretreated HUVEC suspension (8×10^4 cells). After 10 h, tube formation was assessed by staining with FITC and imaging with a fluorescence microscope. The levels of tubes and branch points was quantified in five random fields per insert.

The levels of angiogenic-related genes and proteins, such as VEGF, PDGF, and HIF-1α, in NIR-irradiated HUVECs pre-treated by MnO_2, TA@MnO_2, and CuTA@MnO_2 nanoflakes were determined via RT-PCR and WB analysis. Primer sequences are displayed in Table S1 (Supporting Information).

Preparation of CuTA@MnO_2 Microneedles: CuTA@MnO_2 nanoflakes were homogeneously mixed with a solution comprised of 5 % methacrylated HA and 0.25 % 2-hydroxy-2-methylpropiophenone, resulting in a final concentration of 1.5 mg/mL CuTA@MnO_2 mixture. This mixture was injected into the conical holes of a polydimethylsiloxane-derived microneedle mold and solidified under ultraviolet light (405 nm) for 40 s. Subsequently, 20 % polyvinyl alcohol was added to the bottom of the mold, followed by drying at 40 °C to obtain the CuTA@MnO_2 microneedles. Identical method was applied to obtain MnO_2 and TA@MnO_2 microneedles. And a pure microneedle without nanoflake addition was also prepared for comparison.

The morphology of the CuTA@MnO_2 microneedle was initially photographed, followed by light microscopy and SEM examinations. Quantifications of uniformity and sharpness were performed using ImageJ software based on the obtained images. The photothermal behaviors of the synthesized MnO_2 and CuTA@MnO_2 microneedles were evaluated as described above.

Mechanical Properties: The compressive properties of the CuTA@MnO_2 microneedles were assessed using a Universal Mechanics Tester (Instron, USA). The microneedles were positioned horizontally on a stainless-steel platform with the tips facing upward. The mechanical sensor moved vertically downward at a constant speed of 10 μm/s, and the compressive-strain curve was recorded until a preset load of 80 N was reached.

Insertion Ability: Male Sprague Dawley rats (6–8 weeks old) were purchased from Shanghai Jiagan Biotechnology Co., Ltd (China). All animal experiments were conducted according to the "Guidelines for the Care and Use of Laboratory Animals" and were approved by the Medical Ethics Committee of the First Affiliated Hospital of Shandong First Medical University (SYDWLS [2022] 018). Rats were anesthetized, and

a circular wound defect (10 mm diameter) was created. The CuTA@MnO_2 microneedles were vertically inserted into the wound with a force of 20 N. The treated wound area was then cut longitudinally to prepare frozen sections for HE staining.

Biodegradability: For in vitro degradability assessment, the CuTA@MnO_2 microneedles were initially weighed (M_0). They were then subjected to NIR illumination (808 nm, 1.5 W/cm^2) for 10 min and soaked in PBS solution (pH = 7.4) for 13 days. A microneedle without NIR illumination served as a control. The microneedles were retrieved every other day and weighed (M_n). The degradation rate was determined using the following formula: (M_n/M_0) × 100 %.

For in vivo biodegradability assessment, the CuTA@MnO_2 microneedles were labeled with FITC. A 1 mg/mL FITC solution was added to a mixture of CuTA@MnO_2 as described above. The resulting composite solution was stirred for 24 h, dialyzed for 2 days, and freeze-dried. The composite was then used to fabricate FITC-labeled CuTA@MnO_2 microneedles as described above.

The FITC-labeled CuTA@MnO_2 microneedles were applied to rat skin. The rats were euthanized after 5, 60, and 120 min, and the treated wound tissue was excised for histological section preparation. The fluorescence of the dye-loaded microneedles was analyzed using a fluorescence microscope.

In Vivo Biosafety Assessments: Twenty-one days after inserting various microneedles into the backs of rats (as described above), HE staining was performed to assess the biological safety of different microneedle formulations (pure microneedle, MnO_2 microneedle, TA@MnO_2 microneedle, and CuTA@MnO_2 microneedle) on critical organs, including the heart, liver, spleen, lungs, and kidneys. The PBS group was used as a control.

Treatment of CuTA@MnO_2 Microneedles in a Rat IDW Model: Thirty male Sprague Dawley rats (6–8 weeks old) were induced with type 2 diabetes by administering streptozotocin for one week, resulting in glucose index higher than 16.7 mmol/L. A 10-mm diameter circular wound defect was created in each rat, followed by the application of red fluorescent protein tagged MRSA (20 μL 5 × 10^8 CFU/mL), resulting in an IDW model. Rats meeting the IDW criteria were randomly divided into five groups: Blank, pure microneedle, MnO_2 microneedle, TA@MnO_2 microneedle, and CuTA@MnO_2 microneedle. The microneedle groups received the corresponding treatments, while the Blank group received an injection of 100 μL PBS. The treated wounds were irradiated with an NIR laser (808 nm, 1.5 W/cm^2) for 10 min. Wound size was photographed every other day and quantified the wound closure percentages as previously established [19].

Experimental rats were euthanized on days 7 and 15. Repaired wound tissues were stained with HE to assess epidermal condition, scar length, and complete healing time. In addition, tissues were stained with Masson's trichrome to evaluate collagen regeneration. FISH staining was used to assess bacterial presence and ROS levels. Immunohistochemical CD31 staining was performed to detect angiogenesis, and immunohistochemical collagen III and I staining was conducted to ascertain protein type. The bacterial and ROS intensities, vessel numbers, and the percentages of total collagen fiber, collagen III, and collagen I were quantified in five random fields per insert.

RNA-Sequencing and Data Analysis: RNA-sequencing was conducted in groups of pure microneedle and CuTA@MnO_2 microneedle using standard sequencing procedures (Cloud-seq Company, China). A gene was considered expressed in a sample if its value was equal to or greater than 1. Differentially expressed genes (DEGs) were defined as having a fold change ≥4 and a P value ≤ 0.05. GO and KEGG analysis was performed using DAVID and REVIGO (https://david.ncifc rf.gov; http://revigo.irb.hr/). Target gene screening was based on the GeneCards dataset (https://www.genecards.org/). For each group, three duplicates were collected, and their RNAs were extracted, sequenced, and analyzed.

Statistical Analysis: Statistical analysis was performed using SPSS version 19.0 software. All data, obtained from a minimum of three independent experiments, are presented as mean ± standard deviation (SD). Multiple comparisons were conducted using the Tukey post-hoc test to determine significant differences among groups. Comparisons between multiple groups were performed using two-way ANOVA, and comparisons between two groups were performed using Student's t-test. Statistical significance was marked as $^*p < 0.05$.

CRediT authorship contribution statement

Dong Yan: Writing – original draft, Visualization, Validation, Software, Methodology, Investigation, Formal analysis, Data curation. **Guoqi Cao:** Writing – review & editing, Validation, Methodology, Investigation, Formal analysis, Data curation. **Yikai Gao:** Writing – review & editing, Software, Methodology, Investigation, Formal analysis. **Yiping Wang:** Methodology, Investigation. **Wenqiang Zhang:** Project administration, Funding acquisition. **Kun Wang:** Methodology, Investigation. **Shumei Mao:** Writing – review & editing, Investigation. **Chengde Li:** Writing – review & editing, Validation, Methodology. **Guangdong Zhou:** Supervision, Conceptualization. **Huitang Xia:** Writing – review & editing, Project administration, Funding acquisition, Conceptualization. **Wufei Dai:** Writing – review & editing, Supervision, Data curation, Conceptualization. **Xiaoyu Yan:** Writing – review & editing, Resources, Conceptualization. **Yibing Wang:** Writing – review & editing, Supervision, Project administration, Funding acquisition, Data curation, Conceptualization.

Data availability statement

The data that support the findings of this study are available from the corresponding author upon reasonable request.

Declaration of competing interest

The authors declare no conflict of interest.

Acknowledgements

D. Yan, G. Q. Cao, and Y. K. Gao contributed equal to this work. This research was supported by National Natural Science Foundation of China (81972947 and 82001979), Shandong Provincial Natural Science Foundation (Major Basic Research Program, ZR2019ZD38), Natural Science Foundation of Shandong Province (ZR2020MH381), Academic Promotion Program of Shandong First Medical University (2019LJ005), Shandong First Medical University Culture Foundation (202201-09), and Social Science Planning and Research Project of Shandong Province (21CTQJ08).

Appendix A. Supplementary data

Supplementary data to this article can be found online at https://doi.org/10.1016/j.mtbio.2025.101554.

Data availability

Data will be made available on request.

References

[1] A. Atamna, G. Ayada, A. Akirov, T. Shochat, J. Bishara, A. Elis, QJM : Monthly Journal of the Association of Physicians, 112, 2019, p. 101.
[2] A.E. Louiselle, S.M. Niemiec, C. Zgheib, K.W. Liechty, Transl. Res.: J. Lab. Clin. Med. 236 (2021) 109.
[3] X. Qi, X. Ge, X. Chen, E. Cai, Y. Xiang, H. Xu, Y. Li, Y. Lan, Y. Shi, H. Deng, J. Shen, Adv. Funct. Mater. 34 (2024) 2400489.
[4] V.R. Pasupuleti, C.S. Arigela, S.H. Gan, S.K.N. Salam, K.T. Krishnan, N.A. Rahman, M.S. Jeffree, Oxid. Med. Cell. Longev. (2020) 8878172, 2020.
[5] Y.N. Zhu, J.M. Zhang, J.Y. Song, J. Yang, Z. Du, W.Q. Zhao, H.S. Guo, C.Y. Wen, Q. S. Li, X.J. Sui, L. Zhang, Adv. Funct. Mater. 30 (2020).

[6] a) S. Bowers, E. Franco, Am. Fam. Physician 101 (2020) 159;
b) A. Markiewicz-Gospodarek, M. Kozioł, M. Tobiasz, J. Baj, E. Radzikowska-Büchner, A. Przekora, Int. J. Environ. Res. Publ. Health 19 (2022).
[7] a) V. Vivcharenko, M. Trzaskowska, A. Przekora, Int. J. Mol. Sci. 24 (2023);
b) Z. Wang, X. Liang, G. Wang, X. Wang, Y. Chen, Adv. Mater. (2023), https://doi.org/10.1002/adma.202304738e2304738;
c) W. Hu, W. Wang, Z. Chen, Y. Chen, Z. Wang, Theranostics 14 (2024) 2099.
[8] F. Hu, Q. Gao, J. Liu, W. Chen, C. Zheng, Q. Bai, N. Sun, W. Zhang, Y. Zhang, T. Lu, J. Mater. Chem. B 11 (2023) 2830.
[9] R. Mo, H. Zhang, Y. Xu, X. Wu, S. Wang, Z. Dong, Y. Xia, D. Zheng, Q. Tan, Adv. Drug Deliv. Rev. 195 (2023) 114753.
[10] a)D. Yu, L. Chen, T. Yan, Y. Zhang, X. Sun, G. Lv, S. Zhang, Y. Xu, C. Li, Adv. Healthc. Mater. n/a, 2301985;. b) C. Wang, Y. Zeng, K.F. Chen, J. Lin, Q. Yuan, X. Jiang, G. Wu, F. Wang, Y.G. Jia, W. Li, Bioact. Mater. 27 (2023) 58.
[11] a) M. Yin, J. Wu, M. Deng, P. Wang, G. Ji, M. Wang, C. Zhou, N.T. Blum, W. Zhang, H. Shi, N. Jia, X. Wang, P. Huang, ACS Nano 15 (2021) 17842.b)Z. Chen, L. Zhang, Y. Yang, W. Cheng, L. Tu, Z. Wang, Y. Chen, W. Hu, Adv Funct Mater. n/a, 2417415.
[12] B. Wang, X. Fei, H.F. Yin, X.N. Xu, J.J. Zhu, Z.Y. Guo, J.W. Wu, X.S. Zhu, Y. Zhang, Y. Xu, Y. Yang, L.S. Chen, Small 20 (2024) 2309454.
[13] Q. Lei, D. He, L. Ding, F. Kong, P. He, J. Huang, J. Guo, C.J. Brinker, G. Luo, W. Zhu, Y. Yu, Adv. Funct. Mater. 32 (2022) 2113269.
[14] Y. Wang, Q. Zong, H. Wu, Y. Ding, X. Pan, B. Fu, W. Sun, Y. Zhai, Macromol. Biosci. 23 (2023) e2300332.
[15] A.Q. Zhan, L. Chen, W. Sun, Y. Tang, J. Chen, D.J. Yu, W. Zhang, Mater. Des. 218 (2022).
[16] a) H. Byun, Y. Han, E. Kim, I. Jun, J. Lee, H. Jeong, S.J. Huh, J. Joo, S.R. Shin, H. Shin, Bioact. Mater. 36 (2024) 185;
b) X. Qi, E. Cai, Y. Xiang, C. Zhang, X. Ge, J. Wang, Y. Lan, H. Xu, R. Hu, J. Shen, Adv. Mater. 35 (2023) 2306632.
[17] S. Sisakhtnezhad, M. Rahimi, S. Mohammadi, Biomed. Pharmacother. 163 (2023) 114833.
[18] N.T.H. Nguyen, G.T. Tran, N.T.T. Nguyen, T.T.T. Nguyen, D.T.C. Nguyen, T. V. Tran, Environ. Res. 231 (2023) 116262.
[19] K. Wang, H. Wang, Y. Liu, Z. Li, Mater. Today Commun. 36 (2023) 106870.
[20] a) S.Y.Z. Moghaddam, E. Biazar, J. Esmaeili, B. Kheilnezhad, F. Goleij, S. Heidari, Mini Rev. Med. Chem. 23 (2023) 1320;
b) N. Xu, Y. Yuan, L. Ding, J. Li, J. Jia, Z. Li, D. He, Y. Yu, Burns & Trauma, 10, 2022;
c) N. Xu, Y. Gao, Z. Li, Y. Chen, M. Liu, J. Jia, R. Zeng, G. Luo, J. Li, Y. Yu, Chem. Eng. J. 466 (2023) 143173.
[21] Y. Xu, Y. Luo, Z. Weng, H. Xu, W. Zhang, Q. Li, H. Liu, L. Liu, Y. Wang, X. Liu, L. Liao, X. Wang, ACS Nano 17 (2023) 18732.
[22] W. Chen, W. Xie, Z. Gao, C. Lin, M. Tan, Y. Zhang, Z. Hou, Adv. Sci. 10 (2023) e2303694.
[23] J.C. Nwabuife, C.A. Omolo, T. Govender, J. Contr. Release : Offic. J. Controll. Release Soc. 349 (2022) 338.
[24] Q. Liu, Y. Ren, H. Jia, H. Yuan, Y. Tong, S. Kotha, X. Mao, Y. Huang, C. Chen, Z. Zheng, L. Wang, W. He, ACS Nano 17 (2023) 22527.
[25] Y. Li, R. Fu, Z. Duan, C. Zhu, D. Fan, ACS Nano 16 (2022) 7486.
[26] C. Tu, H. Lu, T. Zhou, W. Zhang, L. Deng, W. Cao, Z. Yang, Z. Wang, X. Wu, J. Ding, F. Xu, C. Gao, Biomaterials 286 (2022) 121597.
[27] a) S. Hu, L. Wang, J. Li, D. Li, H. Zeng, T. Chen, L. Li, X. Xiang, ACS Biomater. Sci. Eng. 9 (2023) 5332;
b) K.G. Abdel-Wahhab, H. Fawzi, F.A. Mannaa, Pathophysiology 23 (2016) 19.
[28] C. Han, M. Barakat, L.A. DiPietro, Cold Spring Harbor Perspect. Biol. 14 (2022).
[29] K. Wang, Y. Liu, H. Wang, Y. Liu, X. Yang, S. Sun, Biomater. Adv. 142 (2022) 213154.
[30] G. Lu, B. Li, L. Lin, X. Li, J. Ban, Biomed. Pharmacother. 173 (2024) 116339.
[31] J. Yang, J. Yang, X. Gong, Y. Zheng, S. Yi, Y. Cheng, Y. Li, B. Liu, X. Xie, C. Yi, L. Jiang, Adv. Healthcare Mater. 11 (2022) e2102547.
[32] S.S. Garg, R. Dubey, S. Sharma, A. Vyas, J. Gupta, Int. J. Biol. Macromol. 247 (2023) 125636.
[33] Y. Yu, P. Li, C. Zhu, N. Ning, S. Zhang, G.J. Vancso, Adv. Funct. Mater. 29 (2019) 1904402.
[34] J.W. Wu, H.F. Yin, X. Song, M. Deng, B. Wang, X. Fei, J.J. Zhu, Z.Y. Guo, H. M. Zhang, W. Chen, Y. Xu, Adv. Funct. Mater. (2024), https://doi.org/10.1002/adfm.202313997.